Journal of Materials Chemistry A

PAPER

View Article Online
View Journal

Cite this: DOI: 10.1039/c6ta06470a

A fascinating multitasking Cu-MOF/rGO hybrid for high performance supercapacitors and highly sensitive and selective electrochemical nitrite sensors†

Mohit Saraf,[a] Richa Rajak[b] and Shaikh M. Mobin*[abc]

Received 29th July 2016
Accepted 9th September 2016

DOI: 10.1039/c6ta06470a

www.rsc.org/MaterialsA

Herein, we report a multitasking Cu-MOF/rGO hybrid, fabricated by simple ultra-sonication of slow diffusion driven Cu-MOF crystals with chemically synthesized reduced graphene oxide (rGO). The molecular structure of the Cu-MOF was authenticated by single crystal X-ray studies. The prepared materials have been probed by various physicochemical characterization techniques. Due to the positive synergistic effects between Cu-MOF crystals and rGO nanosheets, the newly synthesized Cu-MOF/rGO hybrid delivers high charge storage efficiency (685.33 F g^{-1} at 1.6 A g^{-1}), high energy (137.066 W h kg^{-1}) and power density (4800.04 W kg^{-1}) and excellent rate ability (retains 71.01% of its initial capacitance at 8 A g^{-1}). Furthermore, the long cycle life (91.91% after 1000 cycles) of this hybrid indicates its high stability on the electrode surface. Additionally, the electrode modified with the Cu-MOF/rGO hybrid performs exceptionally towards the electrochemical detection of nitrite in a wide dynamic linear range of 3–40 000 μM (R^2 = 0.99911), with a notable detection limit of 33 nm and a high sensitivity of 43.736 μA μM^{-1} cm^{-2}. The versatility of the Cu-MOF/rGO modified electrode can be observed by distinguished selectivity in the presence of some common interfering species and also ability to detect nitrite in real samples.

Introduction

Recently, high-performance supercapacitors and sensor platforms have attracted significant research attention due to the increasing demand for lightweight, highly efficient, sustainable energy sources and ultra-high sensitive and selective diagnosis.[1–7] Supercapacitors are generally categorized into electric double-layer capacitors (EDLCs) and pseudocapacitors based on their charge storage mechanism.[8–13] Recent time has witnessed high energy demand and therefore development of high energy density supercapacitors is the prime focus of research.[4] In this regard, continuous efforts have been made by modifications of electrodes which are made of different materials such as metal nanoparticles, metal oxides (CuO, ZnO, MnO_2, and RuO_2), polymeric materials (polyaniline and polypyrrole) and various carbon materials (graphene, CNTs, and carbon black).[14–22] Apart from energy storage, the other major challenge includes the reliable sensing of biomolecules, anions and metal ions. So far, very few reports have dealt with both energy storage and sensing based on the same material.[1–4] In particular, development of nitrite sensors has been an urgent requirement for the last few years, since the nitrite ion (NO_2^-) has been extensively used in drinking water and vegetables and as a food preserving and fertilizing agent.[23,24] It may cause blue baby syndrome, hypertension, stomach cancer and several other diseases.[23–26] These issues highlight the importance of accurate detection and regular monitoring of toxic nitrite ions.[24–28] Although numerous analytical techniques have been developed for the determination of nitrite,[25–35] most of the techniques are tedious and time-consuming and therefore lack the reliability. In contrast, electrochemical methods have gained significant research interest due to their fascinating features such as simple handling, safety, stability, reliability, rapidity and selectivity.[31–37] Additionally, the traditional electrodes are not capable of the accurate and rapid determination of nitrite due to very high oxidation potential of nitrite.[33–45]

The performance of supercapacitors and sensors primarily depends on the composition and microstructure of the employed electrode materials.[5–8] Concerning the above issues, there is an urgent need to develop such multifunctional

[a]Discipline of Metallurgy Engineering and Materials Science, Indian Institute of Technology Indore, Simrol-453552, India. E-mail: xray@iiti.ac.in; Tel: +91 731 2438 762

[b]Discipline of Chemistry, School of Basic Sciences, Indian Institute of Technology Indore, Simrol-453552, India

[c]Centre for Bioscience and Biomedical Engineering, Indian Institute of Technology Indore, Simrol-453552, India

† Electronic supplementary information (ESI) available. CCDC 1496503. For ESI and crystallographic data in CIF or other electronic format see DOI: 10.1039/c6ta06470a

materials, which can synergistically improve the energy density of supercapacitors and can efficiently detect nitrite in real samples.

In this respect, metal–organic frameworks (MOFs) have shown remarkable performance in various research fields especially in energy storage devices and sensors owing to their crystalline ordered structure with a well-defined tunable pore size, large surface area, high porosity and good thermal stability.[46–53] However, single-phase MOFs show limited performance due to their intrinsic weaker properties such as electrical conductivity, electroactivity, and stability. Therefore, multi-component systems assembling MOFs with materials such as graphene, CNTs, carbon black, *etc.* have been proposed.[46] In this respect, graphene or rGO has emerged as a unique conducting additive for energy storage and sensor applications owing to its high electrical conductivity and remarkable mechanical strength.[47–53] Recently, a solid-type supercapacitor based on a MOF–rGO hybrid coated on carbon fiber paper was proposed.[53] The MOF–rGO combination not only facilitates the utilization of the other active materials, but also enhances the mechanical strength and conductivity of the materials synergistically.[46,47,53]

Herein, we present a novel hybrid of slow diffusion driven Cu-MOFs and rGO nanosheets fabricated by a simple ultrasonication assisted technique. We report for the first time the dual application of the Cu-MOF/rGO hybrid as a (i) supercapacitor electrode material and (ii) electrochemical nitrite sensor. The noteworthy improvement in the performance of the supercapacitor as well as the sensor can be expected as the highly porous Cu-MOF crystals provide a high surface area and the combination of rGO serves to synergistically enhance the conductivity of the hybrid.

Experimental

Chemicals

All chemicals were procured from Merck and used as received. Throughout the synthesis, deionized water (DI water, 18.2 MΩ cm) was employed. A digital ultrasonic cleaner LMUC SERIES (Labman Scientific Instruments) was used in whole experimentation.

Characterization

Powder X-ray diffraction (PXRD) spectra were recorded on a Bruker D2 phaser X-ray diffractometer equipped with Cu-Kα radiation (1.54 Å). Surface morphology was obtained using a field emission scanning electron microscope (FESEM, Hitachi S4700). Transmission electron microscopy (TEM) study was performed on a TECNAI-120 KV system. The N_2 isotherm was measured on a Quantachrome Instrument (Autosorb iQ, version 1.11).

X-ray crystallography

Data were collected at 293(2) K using graphite-monochromated Mo Kα ($\lambda_\alpha = 0.71073$ Å). The data collection was examined using the CrysAlisPro CCD software. The data were collected using standard φ–ω scan techniques and scaled/reduced using CrysAlisPro RED software. The structures were solved by direct methods employing SHELXS-97 and refined by full-matrix least squares with SHELXL-97 on F^2.[54] The positions of all of the atoms were obtained by direct methods. All non-H atoms were refined anisotropically. The remaining H atoms were placed in geometrically constrained positions and refined with isotropic temperature factors, generally $1.2 \times U_{eq}$ of their parent atoms. All of the hydrogen-bonding interactions, mean-plane analyses, and molecular drawings were obtained using the Diamond program (version 3.1d). Solvent molecules were omitted by using the SQUEEZE option in the Platon program.[55]

Electrochemical measurements

All electrochemical experiments were performed on a computer controlled Autolab PGSTAT 204N using NOVA software (version 1.10) at room temperature. The standard three electrode configuration (Ag/AgCl electrode as a reference electrode and platinum wire as a counter electrode) was used. All electrochemical experiments were performed on glassy carbon electrodes (GCEs) of 3 mm diameter. Cyclic voltammetry (CV) measurements for nitrite detection were performed in the voltage window of 0 to +1.2 V in 0.1 M PBS solution and for the supercapacitor test, in the voltage window of −0.5 to 0.7 V in 1 M Na_2SO_4, at different scan rates. Amperometry tests were performed under continuous magnetic stirring conditions. The equations to calculate supercapacitor parameters are given in the ESI.†

Synthesis of reduced graphene oxide (rGO)

The rGO was prepared by modification of Hummer's method. Graphite powder (4 g) and $NaNO_3$ (2 g) were properly mixed and gradually added into concentrated H_2SO_4 (170 mL) on an ice bath. Consequently, $KMnO_4$ (12 g) was added dropwise into the as-formed mixture under magnetic stirring and the temperature was kept below 20 °C. Further, the ice bath was removed and the mixture was kept under continuous stirring for next 18 h which resulted in a brownish coloured viscous mixture. Further, this viscous mixture was diluted with DI water (220 mL) adjusting the temperature below 50 °C. After dilution, the as-formed mixture was treated with 30% H_2O_2 (10 mL), which transformed its colour to bright yellow with bubble formation indicating completion of the reaction and further it was stirred for next 4 h. Finally, the mixture was properly filtered and washed with 10% HCl solution, DI water and ethanol (EtOH) to remove any impurity ions. The filtered product *i.e.* graphite oxide was dried.[57] Later on, graphite oxide (300 mg) was first dispersed in water and then sonicated for 1 h to convert graphite oxide into graphene oxide. Following this, $NaBH_4$ (3 g in 18 mL DI water) was gradually added into the above formed graphene oxide dispersion and the resultant mixture was refluxed at 100 °C for 24 h under stirring conditions. Finally, the obtained product was carefully filtered and washed with DI water and EtOH. The as-formed powder was vacuum dried and denoted as rGO.[56,57]

Synthesis of the Cu-MOF and Cu-MOF/rGO hybrid

In a typical synthesis, the sodium salt of trimesic acid or benzene-1,3,5-tricarboxylic acid (BTC) (0.2 mmol, 46 mg) and $Cu(NO_3)_2 \cdot 3H_2O$ (0.2 mmol, 48 mg) were dissolved separately in 10 mL DI water and EtOH, respectively. Further, 2 mL of metal solution was gradually layered above 2 mL of sodium salt of trimesic acid solution in a narrow glass tube using 1 mL of buffer (1 : 1 DI water and EtOH) solution. Blue block shaped crystals were obtained from the junction of the layer after four days. The Cu-MOF crystals were separated and washed with EtOH and subsequently air dried (yield: 58%). The bulk compound was prepared in powder form by the direct mixing of the ligand mixture with corresponding solution of the metal salts followed by overnight room temperature stirring.[48d] The Cu-MOF/rGO hybrid was prepared by dispersing Cu-MOF and rGO powder in EtOH under ultra-sonication for 30 min by acquiring them in different ratios and after optimization and considering all the factors, 1 : 1 (by weight) was found to be optimum as can be observed from Fig. S1a and b.† Eventually, the final product was harvested by rotary evaporation and subsequent thorough washing with EtOH and DI water as well as drying at 80 °C for 24 h.

Preparation of modified glassy carbon electrodes

Initially, three GCEs were properly polished with alumina slurries and rinsed with DI water several times and dried. Later on, 10 mg powder of each of the Cu-MOF, rGO and Cu-MOF/rGO hybrid was dispersed in EtOH (8 mL) by sonication for half an hour, to form a stable suspension. The CV profiles were obtained at different mass loadings (*i.e.* 2, 4, 5, 6, and 8 μL) for both the supercapacitor and nitrite sensor and after considering all the factors such as current response, charge propagation, CV shape, area under the curve, *etc.*, 5 μL loading (~6.25 μg) was found to be the optimum as can be seen in Fig. S1c and d.† Thereafter, 5 μL of this suspension was drop cast onto the working area of GCEs and dried under infrared lamp irradiation and subsequently the GCE was covered with a smooth layer of Nafion. After drying, the modified GCEs were rinsed three times with DI water and dried before incorporating them into an electrochemical setup.

Results and discussion

Blue coloured crystals of the Cu-MOF were synthesized by a facile reaction of Na_3BTC with $Cu(NO_3)_2 \cdot 3H_2O$ in 1 : 1 molar ratio through a solvent diffusion technique using the EtOH and DI water mixture at room temperature. In most of the earlier reports, the Cu-MOF was prepared under harsh conditions such as high temperature and pressure by solvothermal/hydrothermal techniques.[34,53] In contrast, the present work reports a facile synthesis of the Cu-MOF by a slow diffusion technique at room temperature which is rarely reported.[58] Thereafter, the Cu-MOF was hybridized with rGO by a simple ultra-sonication technique. Scheme 1 shows the schematic formation of the Cu-MOF/rGO hybrid. The as synthesized Cu-MOF/rGO hybrid has been probed by various techniques such as PXRD, SEM, TEM, and BET. Further, the Cu-MOF/rGO hybrid was used as a modifier to the GCE (Cu-MOF/rGO/GCE) to demonstrate its superior electrochemical activity towards supercapacitor application and nitrite sensors.

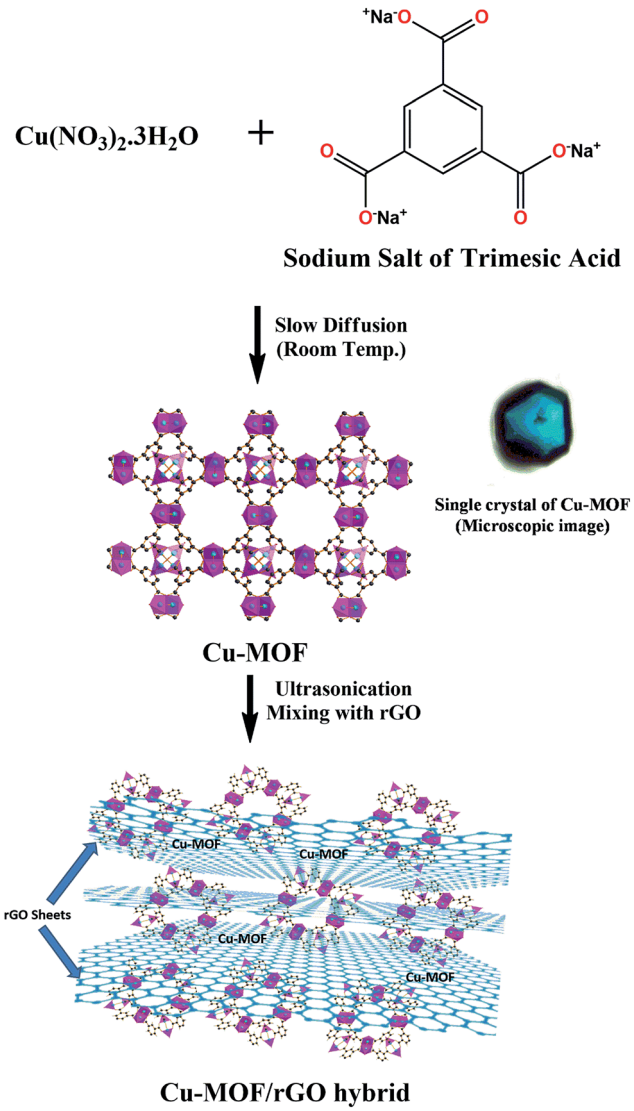

Scheme 1 Schematic synthesis of the Cu-MOF.

Characterization of the Cu-MOF and Cu-MOF/rGO hybrid

The crystallinity and phase purity of the Cu-MOF and Cu-MOF/rGO hybrid were investigated using a powder X-ray diffractometer (PXRD) furnished with Cu-Kα radiation (1.54 Å) in the range of 2–50° (Fig. 1). All diffraction peaks of the Cu-MOF sample can be easily indexed to a cubic crystalline copper trimesate tri-hydrate with an average lattice parameter of 26.3750 Å (JCPDS no. 00-062-1183). Moreover, no peaks related to any impurity ions were detected signifying the high phase purity of the prepared sample (Fig. 1a). Further, the XRD spectrum of Cu-MOF/rGO shows mostly a characteristic of the Cu-MOF only, suggesting that the ultra-sonication mixing of rGO as employed in the present work has not affected the crystal structure of the Cu-MOF (Fig. 1b). The FESEM and TEM images of the Cu-MOF and Cu-MOF/rGO hybrid

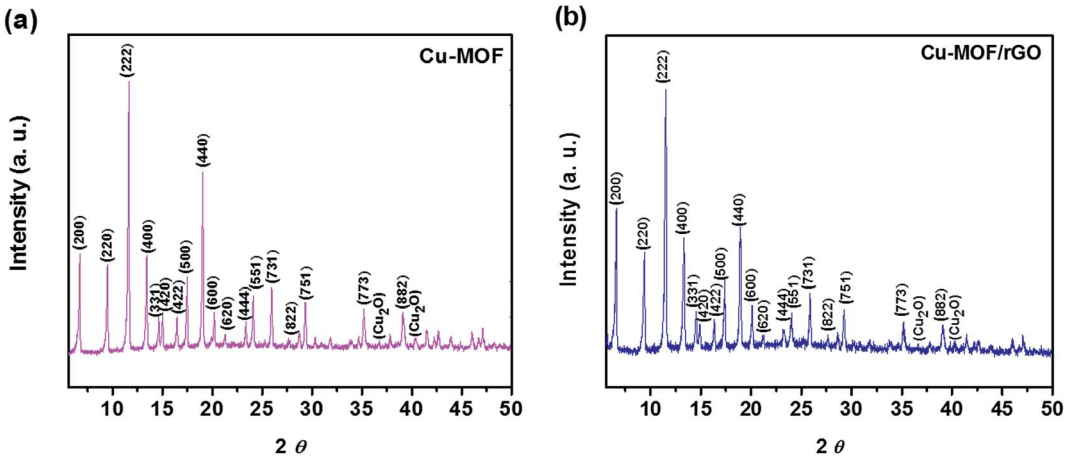

Fig. 1 (a and b) PXRD spectra of the Cu-MOF and Cu-MOF/rGO hybrid.

at different magnifications are shown in Fig. 2. In the SEM images of the Cu-MOF, block-shaped cubic crystals of size varying between 0.5 and 10 μm are clearly visible (Fig. 2a). The SEM images of Cu-MOF crystals at higher magnifications are shown in Fig. 2b and c. TEM images further confirm the presence of block-shaped Cu-MOF crystals (Fig. 2d) and images at higher magnifications reveal the porous structure of these crystals (Fig. 2e and f). Further, the SEM image of the Cu-MOF/rGO hybrid clearly demonstrates the loading of these Cu-MOF crystals within the rGO matrix, where dispersed crystals of the Cu-MOF within the rGO matrix indicate that the ultra-sonication mixing assisted synthesis process can accelerate the dispersion of the materials in the resulting composites (Fig. 2g–i). A histogram of size of Cu-MOF crystals embedded in the hybrid material is also shown in Fig. S2,† which further confirms that the particle size of the Cu-MOF ranges between 0.5 and 10 μm. TEM images of the Cu-MOF/rGO hybrid again confirm the dispersed Cu-MOF crystals embedded within the rGO sheets (Fig. 2j and k). Moreover, the porous structure of these Cu-MOF crystals was maintained even after the formation of the hybrid which reveals the potential of the ultra-sonication-assisted approach for hybrid formation (Fig. 2l). The XRD, SEM and TEM images of rGO are shown in Fig. S3.† It can be assumed from the SEM and TEM images of the Cu-MOF/rGO hybrid that this embedment of Cu-MOF crystals within the rGO matrix may lead to high mechanical strength and high conductivity due to synergistic effects, which ultimately results in high electrochemical performance.

Molecular structure of the Cu-MOF

Single crystal X-ray study discloses the cubic system with $Fm\bar{3}m$ space group of Cu-MOF crystals. Herein, Cu(II) ion forms paddle-wheel units, where the four carboxylate groups lie in equatorial positions and two water molecules occupy the axial positions. Hence, each unit comprises two six-coordinated Cu(II) units possessing a distorted octahedral geometry. Each Cu(II) dimeric unit coordinates with eight oxygens from four carboxylate groups of four BTC^{3-} ligands, which can be unravelled as a 4-connected dimeric metal unit (Fig. 3). Furthermore, each ligand coordinates with three dimeric metal nodes to construct a 3-connected triangular node (Fig. 4a). The Cu-MOF is composed of Cu(II) paddle-wheel units and tri topic BTC ligands to construct an extended 3D-network, which is assembled by 3-connected triangular planar nodes as well as 4-connected rectangular nodes as shown in Fig. 4b and c.[34] The overall Cu-MOF framework is made up of two different types of cage with relatively small pore openings. This porous cage provides additional pathways for charge transfer, which is suitable for achieving enhanced electrochemical response. The measured bond distances of Cu (1)–O (1) and Cu (2)–O (2) are 1.9537 (16) Å and 2.156 (4) Å, respectively and bond angles of O (1)–Cu (1)–O (2) and C (1)–O (1)–Cu (1) are 95.82 (5)° and 122.85 (17)°, respectively. Further, as shown in Fig. 4d, the PXRD pattern of the experimental compound matches well with the simulated one obtained from the single crystal diffractometer, indicating the phase purity of the prepared bulk material. The crystal and refinement data are summarized in Table S1.†

Surface area analysis

The N_2 adsorption/desorption isotherms of the Cu-MOF, rGO and Cu-MOF/rGO hybrid are shown in Fig. 5. The isotherm of the Cu-MOF can be attributed as a typical type I adsorption/desorption isotherm which is typically a characteristic of the microporous material.[51] The Cu-MOF demonstrates a high BET surface area of 1316.246 $m^2\ g^{-1}$, an average pore diameter of 2.32 nm, and a total pore volume of 0.769 $cm^3\ g^{-1}$ (Fig. 5a), and rGO shows a BET surface area of 577.823 $m^2\ g^{-1}$, an average pore diameter of 0.27 nm, and a total pore volume of 1.245 $cm^3\ g^{-1}$ (Fig. 5c). The corresponding Barrett–Joyner–Halenda (BJH) pore size distribution curves are shown in Fig. 5b and d. In contrast, the hybrid Cu-MOF/rGO shows a H3-type hysteresis loop initiating from the relative pressure of 0.39 to that of 0.89 due to the existing mesopores (Fig. 5e).[57] The emergence of the hysteresis loop in the isotherms suggests the presence of mesopores, as further shown in the corresponding BJH pore size distribution curve (Fig. 5f). Moreover, this mesoporous nature of the Cu-MOF/rGO hybrid may play a consequential role in achieving large specific capacitance owing to its ability to facilitate diffusion/ion

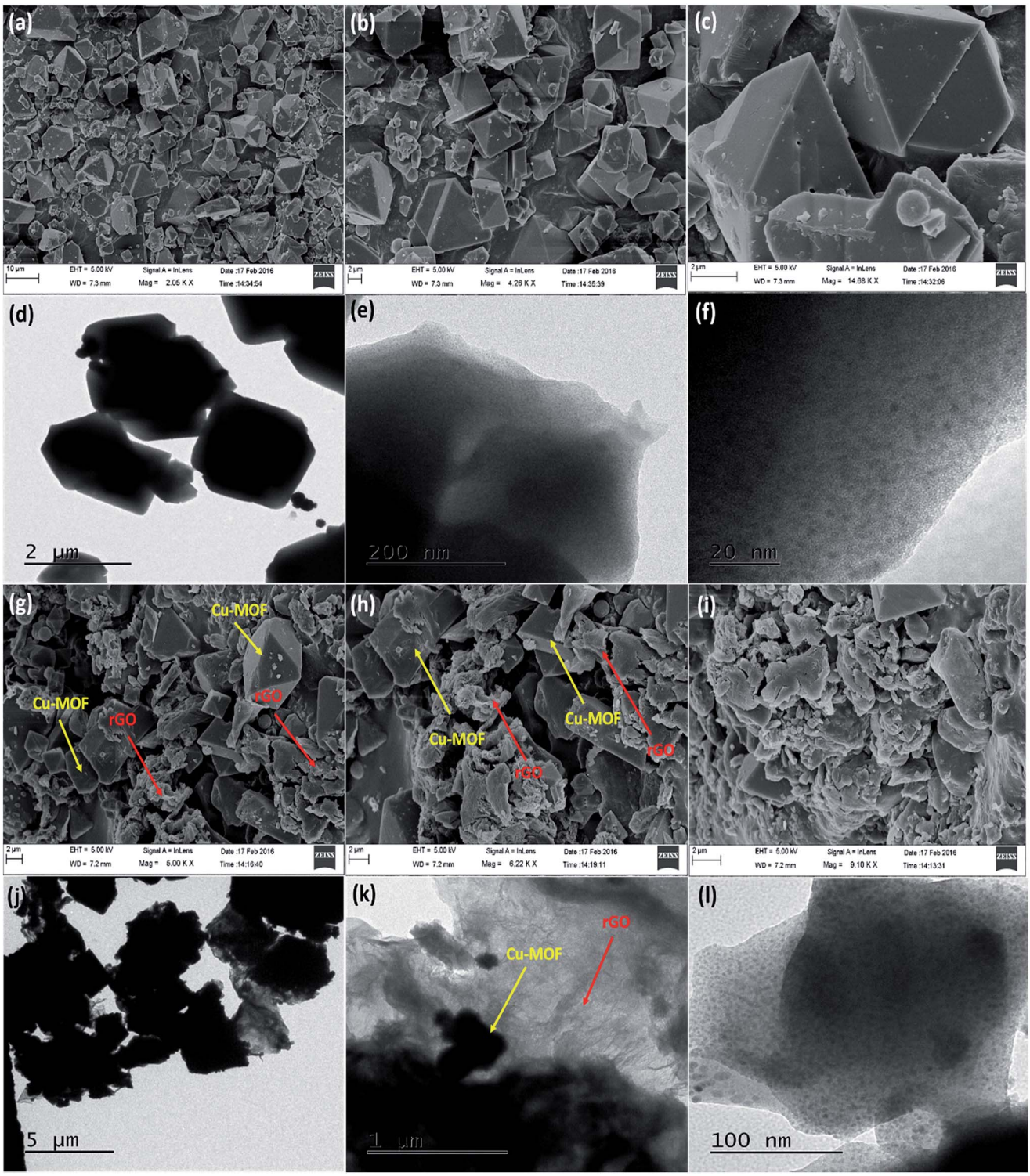

Fig. 2 (a–c) FESEM images of the Cu-MOF, (d–f) TEM images of the Cu-MOF, (g–i) FESEM images of the Cu-MOF/rGO hybrid, and (j–l) TEM images of the Cu-MOF/rGO hybrid, at different magnifications, respectively.

transport and ensuring a high electrochemically active surface area.[49] The hybrid Cu-MOF/rGO has a BET surface area of 1038.71 $m^2\ g^{-1}$, an average pore diameter of 2.78 nm, and a high specific pore volume of 0.726 $cm^3\ g^{-1}$. The high pore volume is beneficial for the fast ion transportation and diffusion during the charge–discharge process and thereby provides more electroactive sites for energy storage. Therefore, the porous structure and large surface area of the Cu-MOF/rGO hybrid are likely to enhance its performance in electrochemical applications.[46,49,53]

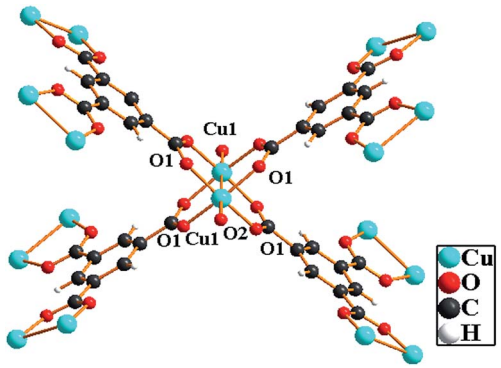

Fig. 3 Molecular structure of the Cu-MOF.

Cu-MOF/rGO/GCE as a supercapacitor electrode material

Electrochemical properties of the Cu-MOF/GCE, rGO/GCE and Cu-MOF/rGO/GCE. The electrochemical properties of electrodes (Cu-MOF/GCE, rGO/GCE and Cu-MOF/rGO/GCE) are evaluated by the cyclic voltammetry (CV) technique at different scan rates (10–500 mV s^{-1}), with potential windows ranging from −0.5 to 0.7 V in 1 M Na_2SO_4 solution, as shown in Fig. 6. It can be observed that the Cu-MOF/GCE shows a pair of redox peaks, whereas the CV spectrum of the rGO/GCE follows an EDLC mechanism and displays nearly rectangular behavior indicating good charge propagation at the GCE surface. In contrast, a highly increased current response/charge transfer and therefore an enhanced integrated area was observed for the Cu-MOF/rGO/GCE due to the synergistic effects between the pseudocapacitive Cu-MOF and electric double layer capacitive rGO, which can be confirmed by comparing the *y*-axis of all three electrodes (Fig. S4†).

The CV profiles of all three electrodes (Cu-MOF/GCE, rGO/GCE and Cu-MOF/rGO/GCE) at different scan rates (10–500 mV s^{-1}) are presented in Fig. 6a–c suggesting that the area under the CV curves increases with the increasing scan rate for all three electrodes. However, the CV integrated area of the Cu-MOF/rGO/GCE is remarkably enhanced compared to that of the rest of the electrodes due to the perfect synergy between Cu-MOF crystals and wrinkled rGO nanosheets, indicating

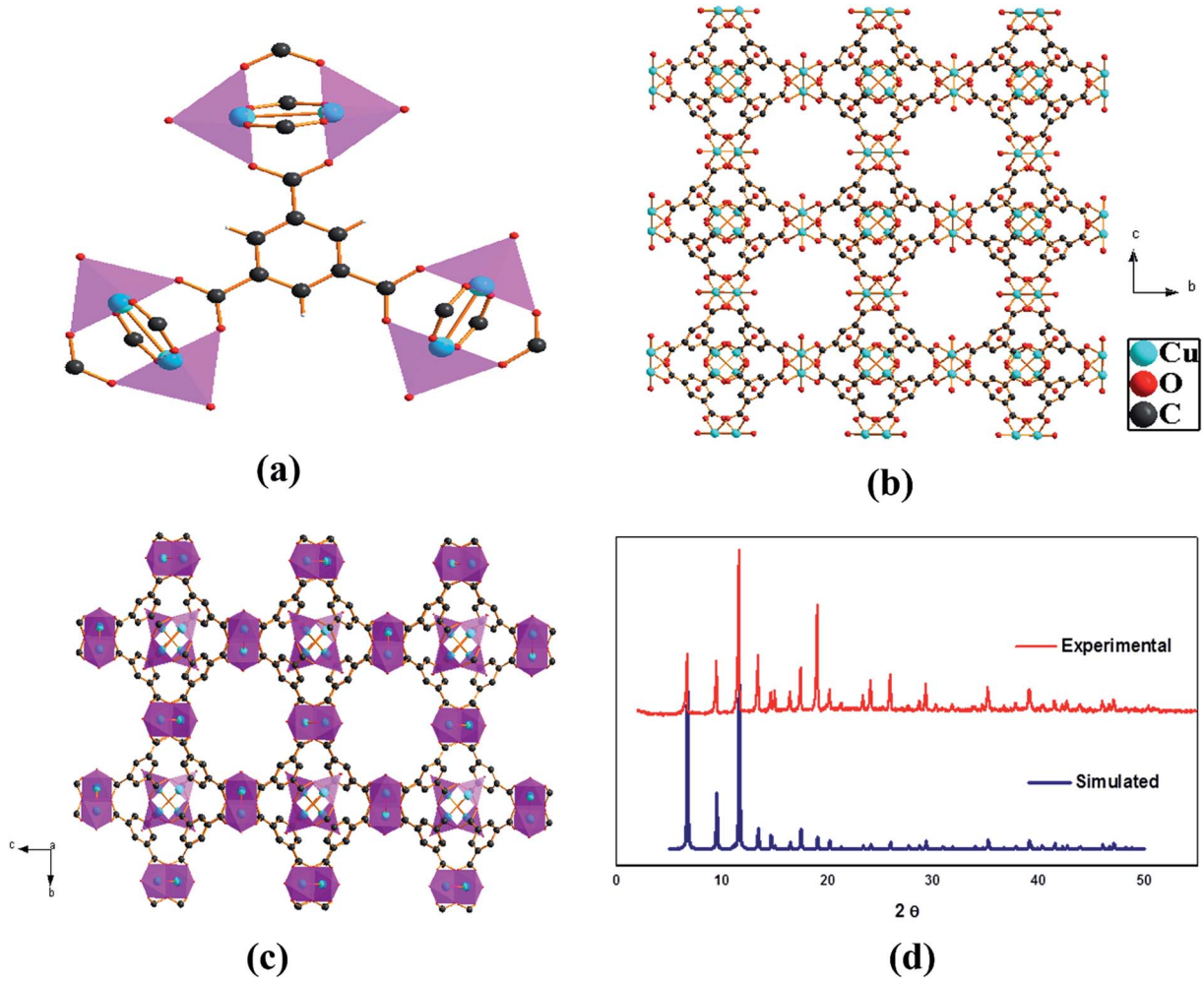

Fig. 4 (a) The organic ligand, BTC^{3-} coordinates with four Cu_2 units and simplified into a 3-connected node, (b & c) 3-D framework built from Cu_2 units and 3-connected ligands along the *a*-axis. Color code: Cu, cyan; O, red; C, dark gray (H atoms and distorted solvent molecules have been omitted for clarity), and (d) X-ray diffraction spectra of the simulated and as-synthesized Cu-MOF.

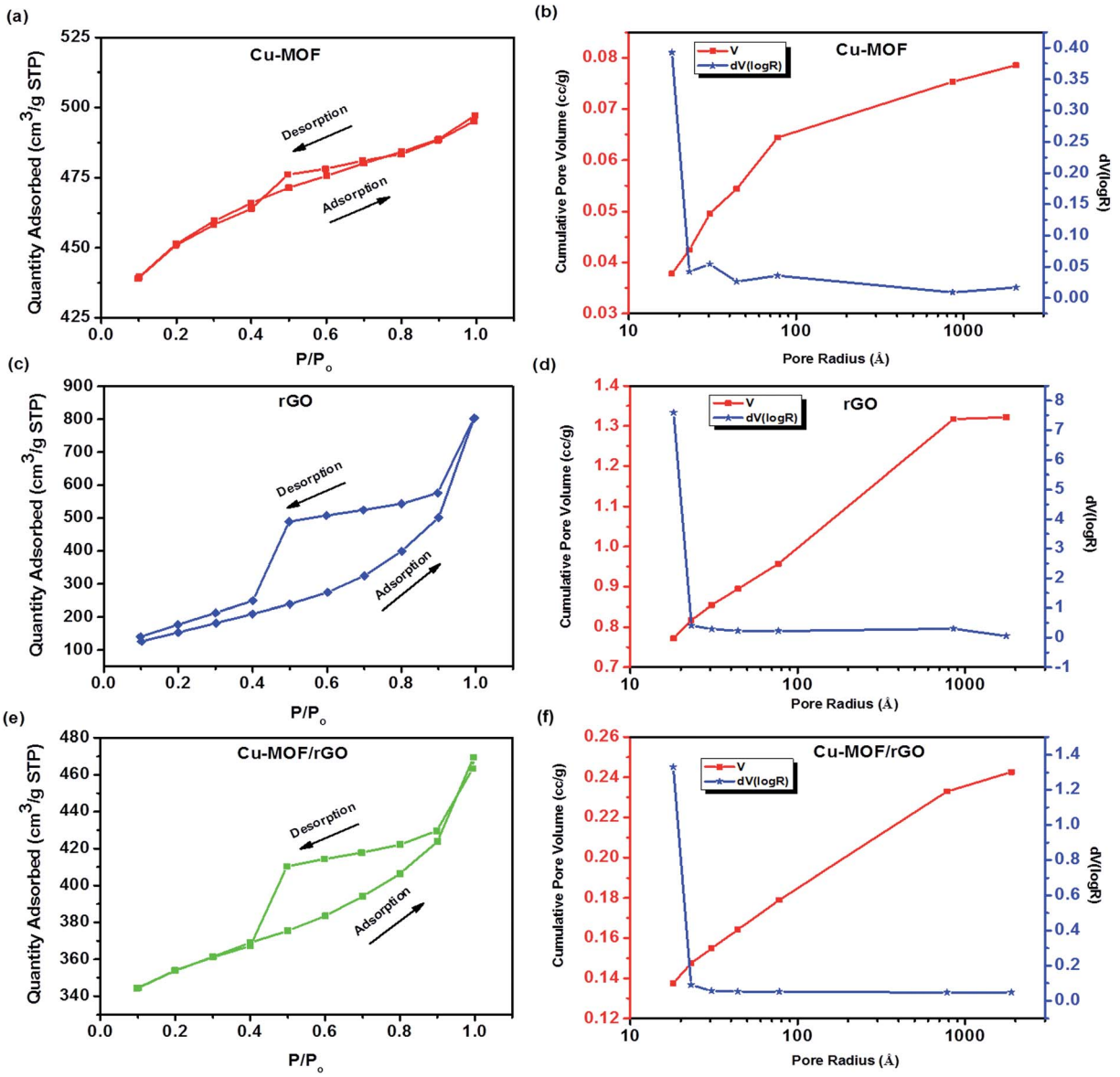

Fig. 5 N_2 adsorption–desorption isotherm and corresponding BJH plots of the (a and b) Cu-MOF, (c and d) rGO and (e and f) Cu-MOF/rGO hybrid, respectively.

a significant improvement in specific capacitance. It should be noted that the Cu-MOF/rGO/GCE displays redox peaks due to the presence of the pseudocapacitive Cu-MOF, but at higher scan rates, it also tries to achieve a quasi-rectangular shape perhaps due to faster diffusion of electrolyte ions leading to enhanced charge storage capacity (Fig. 6c).[15] Herein, the highly porous Cu-MOF crystals generate additional surface area and provide more channels for the charge transfer. However, the Cu-MOF suffers from low conductivity, thereby restricting its application in electrochemical studies. Therefore, the rGO was introduced along with the Cu-MOF to increase the conductivity of the as-formed hybrid. The presence of wrinkles on the crinkly rGO surface prevents restacking and markedly boosts up the conductivity by shortening the ion diffusion path,[57,59] providing an enhanced electrochemical response. As a result, the hybrid shows high porosity, large surface area, better conductivity and large CV integrated area. It is also observed that the Cu-MOF/rGO/GCE maintains a good rectangular shape of the CV curve even at a higher scan rate of 500 mV s^{-1} without any distortion indicating its high rate ability, as well as remarkable electrochemical reversibility.[57] The comparison of CV profiles of all three electrodes at 100 mV s^{-1} scan rate is presented in Fig. 6d, demonstrating that the positive synergism between the Cu-MOF and rGO leads to good charge propagation and an enhanced integrated area due to synergistic contribution of rGO sheets and Cu-MOF crystals.

Galvanostatic charge–discharge (GCD) analyses were also carried out in the potential window of −0.5 to +0.7 V at different applied current densities from 1.6 A g^{-1} to 8 A g^{-1} to

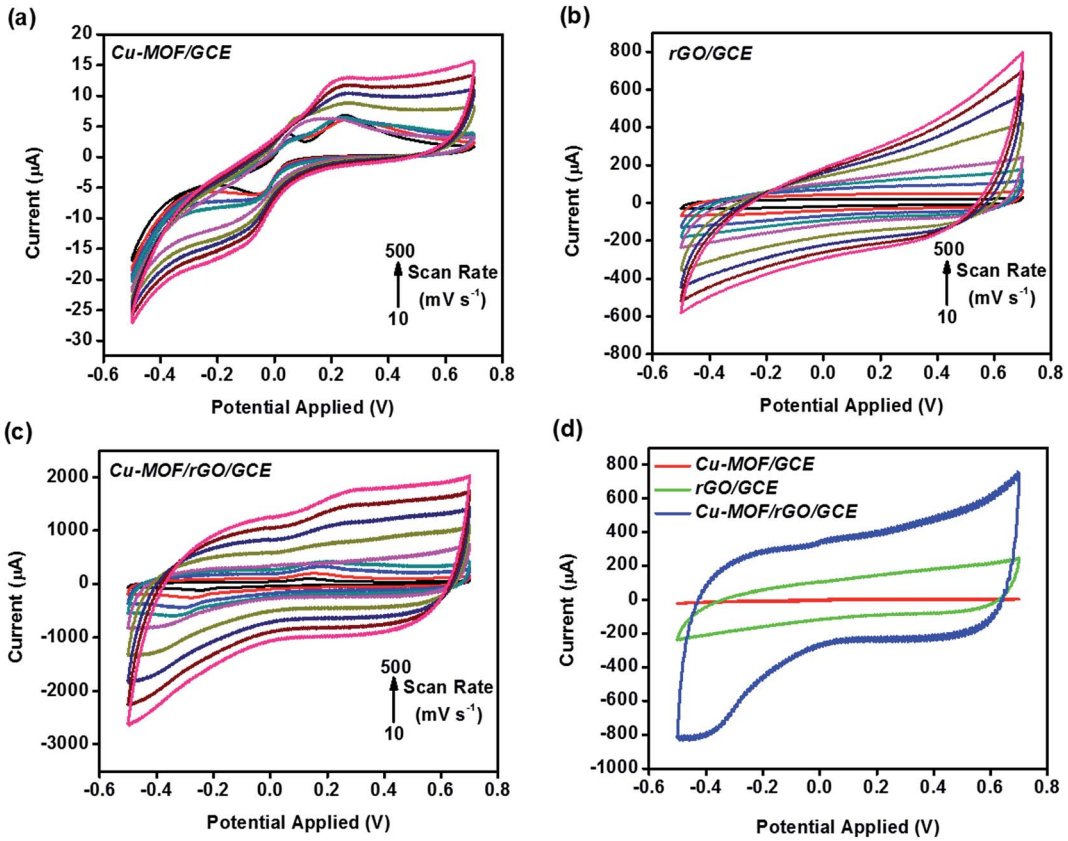

Fig. 6 (a–c) CV profiles of the Cu-MOF/GCE, rGO/GCE and Cu-MOF/rGO/GCE, respectively at different scan rates (10–500 mV s^{-1}) and (d) comparison of the Cu-MOF/GCE, rGO/GCE and Cu-MOF/rGO/GCE at a scan rate of 100 mV s^{-1} in 1 M Na_2SO_4.

evaluate the capacitive performance of all three electrodes (Cu-MOF/GCE, rGO/GCE and Cu-MOF/rGO/GCE) in 1 M Na_2SO_4 solution (Fig. 7). The comparison of charging–discharging profiles of all three electrodes (Cu-MOF/GCE, rGO/GCE and Cu-MOF/rGO/GCE) is shown in Fig. 7d. The longer discharging time of the Cu-MOF/rGO/GCE represents the higher value of specific capacitance than that of the rest of the electrodes and can be attributed to the synergistic effects between the Cu-MOF and rGO. Additionally, the iR drop (voltage drop) of the Cu-MOF/rGO/GCE is comparably smaller than that of the Cu-MOF/GCE, demonstrating the minimized internal resistance after hybrid formation and increased electrical conductivity due to the presence of an EDLC material *i.e.* rGO. The charge–discharge curves of all three electrodes at different current densities (1.6–8 A g^{-1}) are presented in Fig. 7a–c. It can be seen that charge–discharge time reduces upon increasing current density for all three electrodes and results in decreasing specific capacitance. The specific capacitance values for the Cu-MOF/GCE, rGO/GCE and Cu-MOF/rGO/GCE at a current density of 1.6 A g^{-1} are calculated to be 85 F g^{-1}, 410 F g^{-1} and 685.33 F g^{-1}, respectively. The hybrid delivers remarkably high specific capacitance due to the healthy alliance between Cu-MOF crystals and rGO sheets. Further, the rate performance is also analyzed by plotting specific capacitance with reference to current density, suggesting that due to incomplete utilization of active ionic species at high current densities, the charge storage efficiency decreases with increasing current density.[15,57] However, the Cu-MOF/rGO/GCE exhibits high rate ability by retaining 71.01% (486.37 F g^{-1}) of its initial charge storage efficiency even at a high current density of 8 A g^{-1}, better than the rGO/GCE (66.66%) and Cu-MOF/GCE (62.49%), proposing the Cu-MOF/rGO hybrid as a potential material for next generation charge storage devices (Fig. 7e). The maximum energy and power densities of the Cu-MOF/rGO/GCE are evaluated to be 137.066 W h kg^{-1} and 4800.04 W kg^{-1} respectively. Ragone plots of all three electrodes (rGO/GCE, Cu-MOF/GCE and Cu-MOF/rGO/GCE) are presented in Fig. 7f, which demonstrates the remarkable performance of the Cu-MOF/rGO/GCE over other electrodes and shows that energy density decreases and power density increases on increasing current density from 1.6–8 A g^{-1}. Further, the electrochemical stability of the Cu-MOF/rGO/GCE is examined by repeating 1000 charge discharge cycles at a current density of 1.6 A g^{-1} (Fig. 8). The capacitance retention ability of the Cu-MOF/rGO/GCE is determined to be 91.91% after 1000 cycles. This remarkable performance of the Cu-MOF/rGO/GCE can be ascribed to the better transportation of the electrolyte ions within the interconnected open-network structure of the Cu-MOF/rGO/GCE during the fast charge–discharge process and the synergistically induced robust structure of the Cu-MOF/rGO network onto the GCE surface.

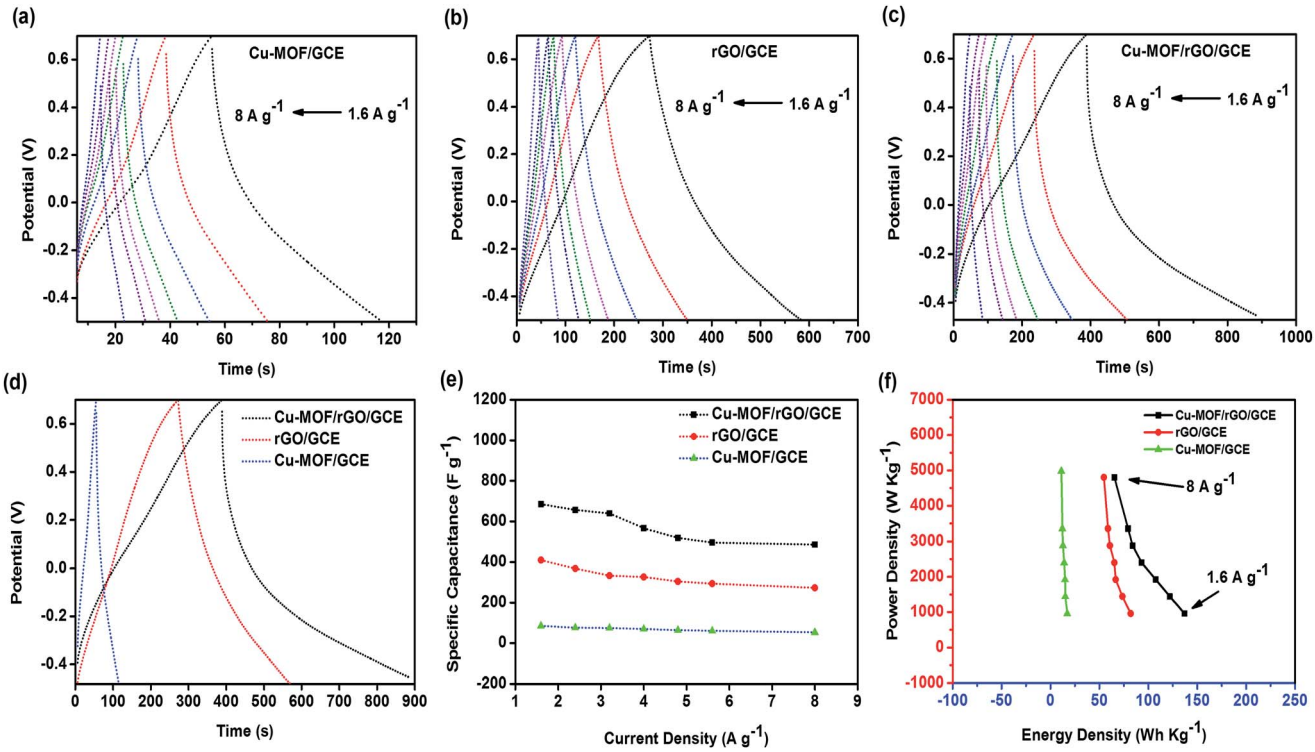

Fig. 7 (a–c) GCD curves of the Cu-MOF/GCE, rGO/GCE and Cu-MOF/rGO/GCE, respectively at different current densities (1.6–8 A g^{-1}) in 1 M Na_2SO_4, (d) comparison of charge–discharge profiles of the Cu-MOF/GCE, rGO/GCE and Cu-MOF/rGO/GCE at a current density of 1.6 A g^{-1}, (e) plots between current density and specific capacitance for the Cu-MOF/GCE, rGO/GCE and Cu-MOF/rGO/GCE, and (f) Ragone plots of the Cu-MOF/GCE, rGO/GCE and Cu-MOF/rGO/GCE.

So far only one report is available describing the supercapacitor performance by introducing a Cu-MOF and rGO hybrid.[53] However, it delivered a specific capacitance of 385 F g^{-1} with energy and power densities of 42 W h kg^{-1} and 3100 W kg^{-1}, respectively, which is comparably quite low as compared to our results *i.e.* specific capacitance of 685.33 F g^{-1} with a very good energy density and power density of 137.066 W h kg^{-1} and 4800.04 W kg^{-1} respectively. The results clearly depict that the Cu-MOF/rGO hybrid (fabricated by a facile slow diffusion process as presented in this work) based supercapacitor has an edge over existing ones.

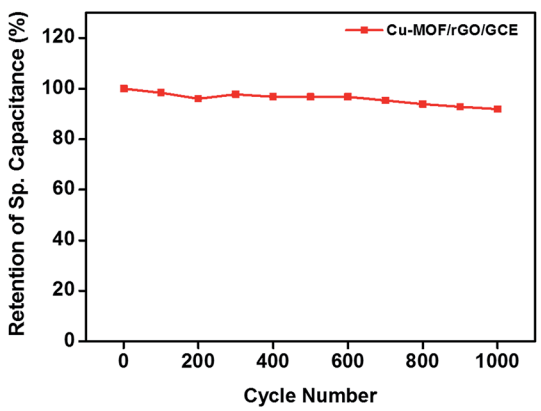

Fig. 8 Retention of specific capacitance with reference to the cycle number for the Cu-MOF/rGO/GCE.

Cu-MOF/rGO/GCE as a nitrite sensor

The fabricated Cu-MOF/rGO hybrid was further explored as a nitrite sensor material. A general scheme of the nitrite sensor is shown in Scheme 2, where the Cu-MOF/rGO/GCE oxidizes the nitrite into nitrate with subsequent generation of an electron. Herein, modified glassy carbon electrodes (Cu-MOF/GCE and Cu-MOF/rGO/GCE) were used as working electrodes to test the electrochemical activity.

Electrocatalytic oxidation of nitrite at the Cu-MOF/rGO/GCE. The electro-oxidation of nitrite for fabricated electrodes has been examined by the cyclic voltammetry (CV) technique in 0.1 M PBS solution as shown in Fig. 9. In the absence of nitrite, the Cu-MOF/rGO/GCE displays the highest current compared to

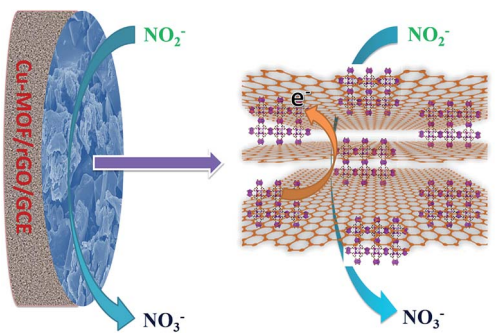

Scheme 2 Schematic of the nitrite sensor.

other electrodes, which is clearly evident from the Fig. 9a, suggesting its high charge transfer capability. Further, in the presence of nitrite, the bare GCE does not show any oxidation peak. In contrast, the Cu-MOF/GCE and Cu-MOF/rGO/GCE both show a significant peak in the presence of nitrite, suggesting the oxidation of nitrite into the nitrate with subsequent generation of an electron (Fig. 9b).[34] However, it can be seen that the latter generates a high current response, suitable for achieving a high electrochemical response. Moreover, it can be observed from the differential pulse voltammetry (DPV) test as shown in Fig. 9c that the nitrite oxidation potential in the case of the Cu-MOF/rGO/GCE has been reduced considerably, demonstrating the positive synergism between the Cu-MOF/rGO hybrid and nitrite. Fig. 9d shows a comparison of the Cu-MOF/rGO/GCE, in the absence and presence of nitrite, producing the high current response with an oxidation peak around 0.76 V in the presence of nitrite, suggesting that the positive synergistic effect between the Cu-MOF and rGO has accelerated the electron transfer rate of electro-oxidation of nitrite. The Cu-MOF/rGO/GCE was further tested at different scan rates and it can be seen from the inset that the anodic current increases linearly with scan rates, suggesting a diffusion-controlled process at the surface of the electrode (Fig. 9e).[60,61] The CVs of the Cu-MOF/rGO/GCE have also been recorded in different concentration ranges of nitrite and it is observed that the Cu-MOF/rGO/GCE shows a sensitive response and current increases linearly with injected concentrations of nitrite. The calibration plot between the current response and nitrite concentrations gives a straight line, demonstrating the potential capability of the Cu-MOF/rGO hybrid to be employed as an electrode material for the nitrite sensor (inset of Fig. 9f). Moreover, it also responds linearly towards higher ranges of injected nitrite concentration as well (Fig. S5†), demonstrating the ability of the Cu-MOF/rGO/GCE to detect nitrite in a wide range.

Amperometric detection of nitrite using the Cu-MOF/rGO/GCE. The electrochemical detection of nitrite has been further investigated by a chrono-amperometry technique under continuous stirring conditions. Fig. 10a shows the amperometric response of the Cu-MOF/rGO/GCE upon successive injections of different concentrations of nitrite under a continuously stirred 0.1 M PBS solution. It can be seen that immediately after the nitrite injection, the Cu-MOF/rGO/GCE responds rapidly towards nitrite oxidation and achieves the steady state current response within 2 s, indicating a faster and sensitive response. The enhanced amperometric currents are linearly proportional to the injected concentrations of nitrite as evident in the calibration plot (inset of Fig. 10a). Moreover, the sensor (Cu-MOF/rGO/GCE) reveals a linear response towards nitrite detection in a wide linear range of 3–40 000 μM ($R^2 = 0.99911$) with a notable detection limit of 33 nm and a high sensitivity of 43.736 μA μM^{-1} cm^{-2}. The sensing performance of the presently fabricated sensor with other reported nitrite sensors is listed in Table 1, from which it can be concluded that the

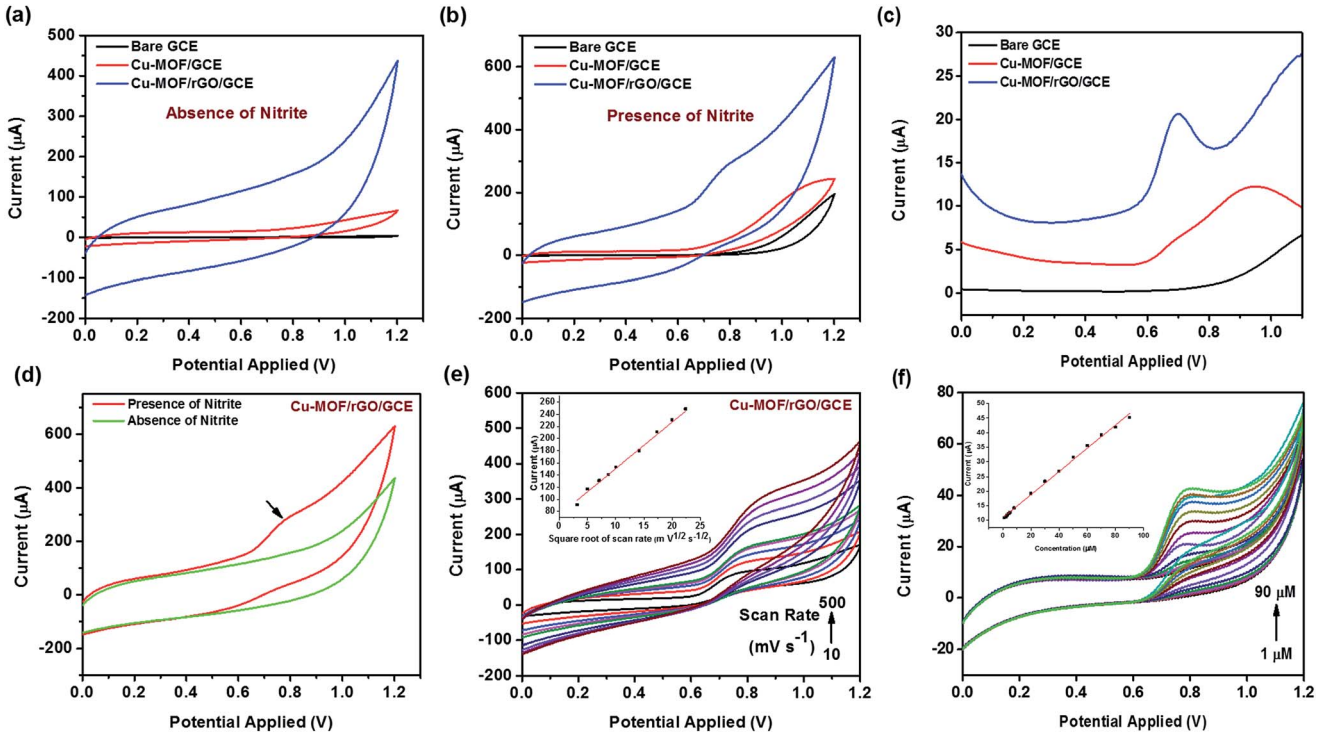

Fig. 9 CV profiles of the bare GCE, Cu-MOF/GCE and Cu-MOF/rGO/GCE (a) in the absence and (b) presence of nitrite, (c) DPV test of the bare GCE, Cu-MOF/GCE and Cu-MOF/rGO/GCE, (d) CV comparison of the Cu-MOF/rGO/GCE in the absence and presence of nitrite, (e) CV at different scan rates (10–500 mV s^{-1}) for the Cu-MOF/rGO/GCE, where the inset shows the linear plot between current and square root of scan rate, and (f) CV profiles of the Cu-MOF/rGO/GCE at different injected concentrations of nitrite, where the inset presents the calibration plot between current and concentration, in 0.1 M PBS solution.

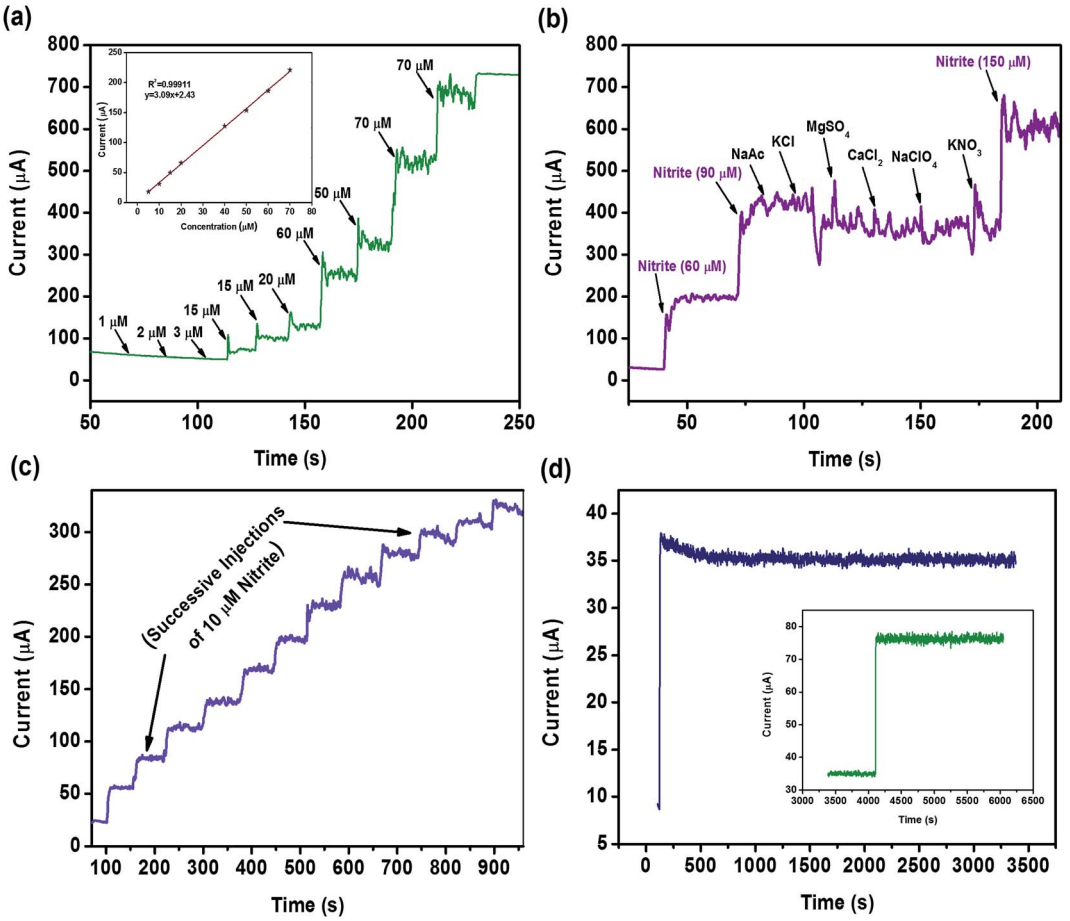

Fig. 10 (a) Amperometric test for the Cu-MOF/rGO/GCE at different injected concentrations of nitrite in 0.1 M PBS, where the inset shows the calibration plot between current and concentration, (b) selectivity test for the Cu-MOF/rGO/GCE towards nitrite in the presence of some common interference species such as NaAC, KCl, $MgSO_4$, $CaCl_2$, $NaClO_4$ and KNO_3, (c) repeatability test for the Cu-MOF/rGO/GCE with successive injections of 10 μM nitrite, and (d) long time amperometric response test for the Cu-MOF/rGO/GCE with 10 μM nitrite injection, where the inset shows the stable long time response before and after second injection of nitrite.

Cu-MOF/rGO based electrode has an edge over almost all other reported nitrite sensors.

Selectivity is also an important factor for nitrite sensors. Therefore, the influence of common interfering ions along with nitrite has been examined by the amperometry test to evaluate the efficacy of the present sensor. Fig. 10b shows the amperometric response of the Cu-MOF/rGO/GCE upon successive additions of nitrite and 500 fold of each possible interferent involving KCl, $MgSO_4$, KNO_3, NaAC, $CaCl_2$ and $NaClO_4$. The Cu-MOF/rGO/GCE exhibits a well defined response towards nitrite additions as can be seen from the first two additions of nitrite, and an insignificant response was observed for other ions. Further addition of higher concentrated nitrite also produces a significant current response, confirming the anti-interfering nature of the Cu-MOF/rGO/GCE. The high stability of the Cu-MOF/rGO/GCE has been probed by repeating the amperometric test for the successive measurements of 10 μM nitrite. It can be seen from Fig. 10c that the current response remains stable even after twelve consecutive injections with a relative standard deviation of 2.5% confirming the repeatability of the sensor. The operation stability of the Cu-MOF/rGO/GCE has also been evaluated by continuous amperometric *i*–*t* curve analysis. The amperometric response of the present sensor retains 97.5% of its initial value over a continuous analysis up to 4000 s with 10 μM nitrite injection (Fig. 10d). In addition to this, further injection of 10 μM nitrite produces the same current response and shows the operation stability for next 2000 s, without any signal distortion (inset of Fig. 10d). The high storage stability of the fabricated sensor was also tested by keeping three different electrodes in air-tight desiccators and the amperometric responses were analyzed twice a day for a period of 15 days. The sensors did not show any noteworthy deviation and confirm that these electrodes can be stored for a long time. Moreover, this test also shows that these electrodes can be revised and a large array of similar electrodes with the same response can be generated.[60–68]

In order to investigate the practical applicability of the present sensor (Cu-MOF/rGO/GCE), pond water spiked with fixed nitrite concentrations was assayed. In a series of analyses, for seven different spiked pond water samples, the concentrations of nitrite were determined with good recoveries as listed in Table S2.† The obtained good recoveries demonstrate that the

Table 1 Comparison of performance of the present sensor with recently reported sensors

Material	Technique	Detection limit (nM)	Linear range (μM)	Sensitivity (μA μM^{-1} cm^{-2})	R^2	Reference
Graphite/β-cyclodextrin hybrid	CA	260 ± 10	0.7–2150	476.25 ± 0.6	0.9944	25
CTAB–GO/MWNT	DPV	1500	5.0–800	—	0.99426	27
Co_3O_4/rGO	CA	140	1–380	29.5	0.9992	28
PEDOT/AuNP	CA	60	0.2–1400	—	0.998	29
MWCNTs–TiN/Cyt c	CA	1.4	1–2000	121.5	0.9994	30
Hexagonal BN whiskers	CA	101 and 478	10–6300 to 20–5200	—	0.997 and 0.991	31
rGO	CA	1000	8.9 to 167	0.0267	0.9990	32
EAG	CA	38	0.1–16 400	126.0	0.9955	33
rGO/MWNT/Pt Mb	CA	—	100–12 000	0.1651(±0.026)	0.989	36
AuNPs/carbon paper	CA	93	1–100	0.08138 and 0.0476	0.99883 and 0.99789	64
rGO/AeNPs/poly(PyY)	CA	12	0.1–1000	13.5	0.9989	65
Au–rGO/PDDA nanohybrid	DPV	40	0.05–8.5	—	0.9964	66
Polyhedral oligomeric silsesquioxane/rGO nanohybrid	CA	80	0.5–120 000	0.255	0.9991	67
rGO/Pd	DPV	230	1–1000	—	0.9912	68
Cu-MOF/rGO hybrid	**CA**	**33**	**3–40 000**	**43.736**	**0.99911**	**This work**

fabricated sensor (Cu-MOF/rGO/GCE) is a potential candidate for real sample analysis. The recovery percent (% R) of pond water samples was determined using the following relationship.[26]

$$\%\ R = \frac{\text{result of spiked sample} - \text{result of unspiked sample}}{\text{known spike added concentration}} \times 100\%$$

The recoveries of nitrite for all concentrations fall in the range of 100–120%, authorizing the suitability of the proposed system for the determination of nitrite in real samples as well.

Conclusions

In summary, a novel and multitasking Cu-MOF/rGO hybrid of slow diffusion grown Cu-MOF powder and chemically produced rGO has been synthesized by a facile ultra-sonication assisted method. The presented supercapacitor provides a maximum specific capacitance of 685.33 F g^{-1} at a current density of 1.6 A g^{-1} by virtue of the synergistically induced robust Cu-MOF/rGO hybrid. Moreover, it delivers high energy and power density and excellent rate performance with long cycle life. The comparison of the present supercapacitor with those reported in the literature clearly indicates its edge over existing ones. In addition to this, the fabricated hybrid display a remarkable sensitive response towards electrochemical detection of nitrite in a wide dynamic linear range of 3–40 000 μM (R^2 = 0.99911), with a notable detection limit of 33 nm, high sensitivity of 43.736 μA μM^{-1} cm^{-2} and distinguished sensitivity in the presence of common interfering agents. The comparison of the Cu-MOF/rGO hybrid based nitrite sensor with other reported sensors highlights its superiority over all other reported sensors. Thus, Cu-MOF/rGO based electrodes show a futuristic approach towards energy storage as well as development of highly selective and sensitive nitrite sensors.

Acknowledgements

S. M. M acknowledges CSIR, New Delhi and IIT Indore for providing funding and Sophisticated Instrumentation Centre (SIC), IIT Indore for all the characterization facilities. The authors gratefully acknowledge Advance Imaging Center, IIT Kanpur for TEM facility. M. S. thanks MHRD, New Delhi, India for providing fellowship. M. S. also thanks Mr Kaushik Natarajan for helpful discussion.

References

1 S. Liu, K. S. Hui and K. N. Hui, *ACS Appl. Mater. Interfaces*, 2016, **8**, 3258–3267.
2 B. Zhao, T. Wang, L. Jiang, K. Zhang, M. M. F. Yuen, J.-B. Xu, X.-Z. Fu, R. Sun and C.-P. Wong, *Electrochim. Acta*, 2016, **192**, 205–215.
3 N. Hui, F. Chai, P. Lin, Z. Song, X. Sun, Y. Li, S. Niu and X. Luo, *Electrochim. Acta*, 2016, **199**, 234–241.
4 V. Veeramani, B. Dinesh, S.-M. Chen and R. Saraswathi, *J. Mater. Chem. A*, 2016, **4**, 3304–3315.
5 A. Burke, *J. Power Sources*, 2000, **91**, 37–50.
6 S. Feng, W. Li, J. Wang, Y. Song, A. A. Elzatahry, Y. Xia and D. Zhao, *Nanoscale*, 2014, **6**, 14657–14661.
7 H. Niu, D. Zhou, X. Yang, X. Li, Q. Wang and F. Qu, *J. Mater. Chem. A*, 2015, **3**, 18413–18421.
8 L. L. Zhang and X. S. Zhao, *Chem. Soc. Rev.*, 2009, **38**, 2520–2531.
9 J. R. Miller and P. Simon, *Science*, 2008, **321**, 651–652.
10 P. Simon and Y. Gogotsi, *Nat. Mater.*, 2008, **7**, 845–854.
11 M. Winter and R. J. Brodd, *Chem. Rev.*, 2004, **104**, 4245–4269.
12 L. L. Zhang, R. Zhou and X. Zhao, *J. Mater. Chem.*, 2010, **20**, 5983–5992.
13 G. Wang, L. Zhang and J. Zhang, *Chem. Soc. Rev.*, 2012, **41**, 797–828.

14 J. Chen, J. Xu, S. Zhou, N. Zhao and C.-P. Wong, *J. Mater. Chem. A*, 2015, **3**, 17385–17391.
15 R. A. Dar, G. A. Naikoo, P. K. Kalambate, L. Giri, F. Khan, S. P. Karna and A. K. Srivastava, *Electrochim. Acta*, 2015, **163**, 196–203.
16 X. Zhang, W. Shi, J. Zhu, D. J. Kharistal, W. Zhao, B. S. Lalia, H. H. Hng and Q. Yan, *ACS Nano*, 2011, **5**, 2013–2019.
17 B. Zhao, P. Liu, H. Zhuang, Z. Jiao, T. Fang, W. Xu, B. Lu and Y. Jiang, *J. Mater. Chem. A*, 2013, **1**, 367–373.
18 C. Yuan, X. Zhang, L. Su, B. Gao and L. Shen, *J. Mater. Chem.*, 2009, **19**, 5772–5777.
19 X. Qing, S. Liu, K. Huang, K. Lv, Y. Yang, Z. Lu, D. Fang and X. Liang, *Electrochim. Acta*, 2011, **56**, 4985–4991.
20 X. Zhang, Y. Zhao and C. Xu, *Nanoscale*, 2014, **6**, 3638–3646.
21 J. Yan, E. Khoo, A. Sumboja and P. S. Lee, *ACS Nano*, 2010, **4**, 4247–4255.
22 X.-H. Xia, J.-P. Tu, Y.-J. Mai, X.-L. Wang, C.-D. Gu and X.-B. Zhao, *J. Mater. Chem.*, 2011, **21**, 9319–9325.
23 X. R. Li, F. Y. Kong, J. Liu, T. M. Liang, J. J. Xu and H. Y. Chen, *Adv. Funct. Mater.*, 2012, **22**, 1981–1988.
24 P. Li, Y. Ding, A. Wang, L. Zhou, S. Wei, Y. Zhou and T. Lu, *ACS Appl. Mater. Interfaces*, 2013, **5**, 2255–2260.
25 S. Palanisamy, B. Thirumalraj and S.-M. Chen, *J. Electroanal. Chem.*, 2016, **760**, 97–104.
26 W. Lijinsky, E. Conrad and R. V. D. Bogart, *Nature*, 1972, **239**, 165–167.
27 Y. J. Yang and W. Li, *Biosens. Bioelectron.*, 2014, **56**, 300–306.
28 Y. Haldorai, J. Y. Kim, A. T. E. Vilian, N. S. Heo, Y. S. Huh and Y.-K. Han, *Sens. Actuators, B*, 2016, **227**, 92–99.
29 P. Lin, F. Chai, R. Zhang, G. Xu, X. Fan and X. Luo, *Microchim. Acta*, 2016, **183**, 1235–1241.
30 Y. Haldorai, S.-K. Hwang, A.-I. Gopalan, Y. S. Huh, Y.-K. Han, W. Voit, G. Sai-Anand and K.-P. Lee, *Biosens. Bioelectron.*, 2016, **79**, 543–552.
31 W. Luo, T. Yang, L. Su, K.-C. Chou and X. Hou, *RSC Adv.*, 2016, **6**, 27767–27774.
32 V. Mani, A. P. Periasamy and S.-M. Chen, *Electrochem. Commun.*, 2012, **17**, 75–78.
33 S. Palanisamy, C. Karuppiah, S.-M. Chen and P. Periakaruppan, *J. Electroanal. Chem.*, 2014, **727**, 34–38.
34 B. Yuan, J. Zhang, R. Zhang, H. Shi, N. Wang, J. Li, F. Ma and D. Zhang, *Sens. Actuators, B*, 2016, **222**, 632–637.
35 A. Afkhami, F. S. Felehgari, T. Madrakian and H. Ghaedi, *Biosens. Bioelectron.*, 2014, **51**, 379–385.
36 V. Mani, B. Dinesh, S. M. Chen and R. Saraswathi, *Biosens. Bioelectron.*, 2014, **53**, 420–427.
37 D. Ye, L. Luo, Y. Ding, Q. Chen and X. Liu, *Analyst*, 2011, **136**, 4563–4569.
38 L. Cong, J. Y. Zhao and X. Y. Yan, *Analyst*, 2015, **140**, 1913–1920.
39 D. Ye, L. Luo, Y. Ding, B. Liu and X. Liu, *Analyst*, 2012, **137**, 2840–2845.
40 T. Zhang, H. Fan and Q. Jin, *Talanta*, 2010, **81**, 95–99.
41 G. H. Chen, D. X. Yuan, Y. M. Huang, M. Zhang and M. Bergman, *Anal. Chim. Acta*, 2008, **620**, 82–88.
42 M. Saraf, P. Kumar, G. Kedawat, J. Dwivedi, S. A. Vithayathil, N. Jaiswal, B. A. Kaipparettu and B. K. Gupta, *Inorg. Chem.*, 2015, **54**, 2616–2625.
43 Inamuddin, K. Ahmad and M. Naushad, *Int. J. Hydrogen Energy*, 2014, **39**, 7417–7421.
44 M. Zhang, Z. Zhang, D. X. Yuan, S. C. Feng and B. M. Liu, *Talanta*, 2011, **84**, 443–450.
45 B. R. Kozub, N. V. Rees and R. G. Compton, *Sens. Actuators, B*, 2010, **143**, 539–546.
46 Y. Zhang, X. Bo, C. Luhana, H. Wang, M. Li and L. Guo, *Chem. Commun.*, 2013, **49**, 6885–6887.
47 N. A. Travlou, K. Singh, E. Rodriguez-Castellon and T. J. Bandosz, *J. Mater. Chem. A*, 2015, **3**, 11417–11429.
48 (*a*) B. Ramaraju, C.-H. Li, S. Prakash and C.-C. Chen, *Chem. Commun.*, 2016, **52**, 946–949; (*b*) Y. Wu, A. Kobayashi, G. J. Halder, V. K. Peterson, K. W. Chapman, N. Lock, P. D. Southon and C. J. Kepert, *Angew. Chem.*, 2008, **120**, 9061–9064; (*c*) C.-Y. Sun, S.-X. Liu, D.-D. Liang, K.-Z. Shao, Y.-H. Ren and Z.-M. Su, *J. Am. Chem. Soc.*, 2009, **131**, 1883–1888; (*d*) K. Tomar, R. Rajak, S. Sanda and S. Konar, *Cryst. Growth Des.*, 2015, **15**, 2732–2741; (*e*) J.-L. Zhuang, D. Ceglarek, S. Pethuraj and A. Terfort, *Adv. Funct. Mater.*, 2011, **21**, 1442–1447.
49 Y. Liu, Y. Zhang, J. Chen and H. Pang, *Nanoscale*, 2014, **6**, 10989–10994.
50 Y. Wang, Y. Wu, J. Xie and X. Hu, *Sens. Actuators, B*, 2013, **177**, 1161–1166.
51 H. Hosseini, H. Ahmar, A. Dehghani, A. Bagheri, A. R. Fakhari and M. M. Amini, *Electrochim. Acta*, 2013, **88**, 301–309.
52 H. Hosseini, H. Ahmar, A. Dehghani, A. Bagheri, A. Tadjarodi and A. R. Fakhari, *Biosens. Bioelectron.*, 2013, **42**, 426–429.
53 P. Srimuk, S. Luanwuthi, A. Krittayavathananon and M. Sawangphruk, *Electrochim. Acta*, 2015, **157**, 69–77.
54 G. M. Sheldrick, *Acta Crystallogr., Sect. A: Found. Crystallogr.*, 2008, **64**, 112; G. M. Sheldrick, *Shelx97, Program for Crystal Structure Solution and Refinement*, University of Gottingen, Goettingen, Germany, 1997.
55 A. K. Saini, M. Srivastava, V. Sharma, V. Mishra and S. M. Mobin, *Dalton Trans.*, 2016, **45**, 3927–3935.
56 X. Zhu, Y. Zhu, S. Murali, M. D. Stoller and R. S. Ruoff, *ACS Nano*, 2011, **5**, 3333–3338.
57 M. Saraf, R. A. Dar, K. Natarajan, A. K. Srivastava and S. M. Mobin, *ChemistrySelect*, 2016, **1**, 2826–2833.
58 D. J. Tranchemontagne, J. R. Hunt and O. M. Yaghi, *Tetrahedron*, 2008, **64**, 8553–8557.
59 C. Liu, Z. Yu, D. Neff, A. Zhamu and B. Z. Jang, *Nano Lett.*, 2010, **10**, 4863–4868.
60 Y. Bai, R. B. Rakhi, W. Chen and H. N. Alshareef, *J. Power Sources*, 2013, **233**, 313–319.
61 M. Saraf, K. Natarajan and S. M. Mobin, *Dalton Trans.*, 2016, **45**, 5833–5840.
62 A. Deep, M. Saraf, Neha, S. K. Bharadwaj and A. L. Sharma, *Electrochim. Acta*, 2014, **146**, 301–306.
63 B. J. Sanghavi, S. M. Mobin, P. Mathur, G. K. Lahiri and A. K. Srivastava, *Biosens. Bioelectron.*, 2013, **39**, 124–132.

64 Y. Wan, Y. F. Zheng, H. Y. Yinc and X. C. Song, *New J. Chem.*, 2016, **40**, 3635–3641.
65 K. Dağcı and M. Alanyalıoğlu, *ACS Appl. Mater. Interfaces*, 2016, **8**, 2713–2722.
66 S. Jiao, J. Jin and L. Wang, *Sens. Actuators, B*, 2015, **208**, 36–42.
67 W. Bai, Q. Sheng and J. Zheng, *Talanta*, 2016, **150**, 302–309.
68 L. Fu, S. Yu, L. Thompson and A. Yu, *RSC Adv.*, 2015, **5**, 40111–40116.